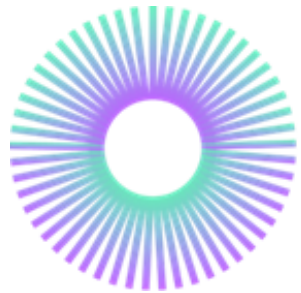




Universidad Internacional
Menéndez Pelayo



Master's Degree in Quantum Technologies

Academic year: 2024 - 2025

Free-Space Quantum Key Distribution under Atmospheric Fluctuations

Student: Gehad Mostafa Hasan Eldibany

Supervisors: Daniel Balado Souto, Veronica Fernandez Marmol

Abstract

Free-space quantum key distribution (QKD) is essential for global quantum communications due to its efficiency over larger distances unlike the fiber-based approach which is limited by exponential photon loss. Satellite-to-ground links, however, are prone to atmospheric effects including absorption, scattering, turbulence-induced beam wander, broadening, scintillation, wavefront aberrations, and background noise. These factors reduce channel transmittance and increase the quantum bit error rate (QBER), which affects the secret key rate (SKR) and link availability.

We present here a turbulence-informed framework to analyze the atmospheric effects on free-space QKD performance and propose mitigation strategies at the operational parameter and receiver levels. We consider a downlink geometry implementing the BB84 protocol and link the atmospheric effects to QKD performance metrics analytically and numerically. Optimization analyses are performed for wavelength, beam waist, ground station altitude, and receiver aperture size, taking into account the relevant trade-offs. Setting the operational wavelength to 1550 nm and the initial beam waist to 0.1 and having a receiver aperture radius \approx 30 cm were found to improve the channel transmittance.

An optical front-end design is proposed for the receiver using a Schmidt–Cassegrain telescope, a quadrant detector, and a fast steering mirror for tip/tilt correction. The proposed optics mitigate the turbulence effects and could achieve a near diffraction-limited by monitoring the focal-plane displacements and compensating and correcting for beam wander and low order aberrations, which reduces QBER. Future work may address high-order aberrations and background noise, particularly in daylight, and using optimization and prediction algorithms to better enhance the performance under atmospheric fluctuations.

Resumen

La distribución de clave cuántica (QKD) en espacio libre es esencial para las comunicaciones cuánticas globales debido a su eficiencia a grandes distancias, a diferencia del enfoque basado en fibra, que se ve limitado por la pérdida exponencial de fotones. Sin embargo, los enlaces satélite-tierra son propensos a efectos atmosféricos, como absorción, dispersión, desplazamiento del haz inducido por turbulencia, ensanchamiento, centelleo, aberraciones del frente de onda y ruido de fondo. Estos factores reducen la transmitancia del canal y aumentan la tasa de error de bits cuántico (QBER), lo que afecta la tasa de clave secreta (SKR) y la disponibilidad del enlace.

Presentamos un marco basado en la turbulencia para analizar los efectos atmosféricos en el rendimiento de la QKD en espacio libre y proponer estrategias de mitigación a nivel de parámetros operativos y del receptor. Consideramos una geometría de enlace descendente que implementa el protocolo BB84 y vinculamos los efectos atmosféricos con las métricas de rendimiento de la QKD analítica y numéricamente. Se realizan análisis de optimización para la longitud de onda, la cintura del haz, la altitud de la estación terrestre y el tamaño de la apertura del receptor, considerando las compensaciones pertinentes. Se observó que establecer la longitud de onda operativa en 1550 nm y la cintura inicial del haz en 0,1, junto con un radio de apertura del receptor de \approx 30 cm, mejoraba la transmitancia del canal.

Se propone un diseño óptico frontal para el receptor que utiliza un telescopio Schmidt-Cassegrain, un detector de cuadrante y un espejo de dirección rápida para la corrección de la inclinación. La óptica propuesta mitiga los efectos de la turbulencia y podría lograr una difracción casi limitada mediante la monitorización de los desplazamientos del plano focal y la compensación y corrección de la desviación del haz y las aberraciones de bajo orden, lo que reduce la QBER.

En futuros trabajos se podría abordar la aberración de alto orden y el ruido de fondo, especialmente a la luz del día, y utilizar algoritmos de optimización y predicción para optimizar el rendimiento bajo fluctuaciones atmosféricas.

Contents

1	Introduction	4
2	Protocol and Geometry	5
2.1	The BB84 Protocol	5
2.2	Geometric Model of the Free-space QKD Downlink	6
3	Atmospheric Effects on Free-Space QKD	6
3.1	Attenuation	6
3.2	Beam wandering	8
3.3	Beam broadening	10
3.4	Scintillation	11
3.5	Wavefront Aberrations	12
3.6	Background Noise	13
3.7	Impact on QKD metrics	14
4	System-Level Mitigation Strategies	15
4.1	Wavelength Selection	15
4.2	Beam Waist Optimization	16
4.3	Ground Instrument Altitude h_0	19
4.4	Receiver Aperture Radius a_R	20
4.5	Beam Wander and Focal Plane Displacement	23
5	Receiver Optical Design	24
5.1	Telescope	24
5.2	Quadrant Detector	25
5.3	Tip/Tilt Mirror	25
A	fiber attenuation and link efficiency	27

1 Introduction

Quantum cryptography provides unconditional security guaranteed by the laws of quantum mechanics and surpasses the classical mathematical approaches with the ability to detect interception and passive eavesdropping. One promising quantum method is the QKD, which secures the exchange of encryption keys via quantum channels. Since the first QKD protocol was proposed using polarized single photons [3], there have been many implementations to prove QKD feasibility and security over large distances to realize a global QKD network.

Optical fibers have been widely used in modern networks as they provide transmission channels with low loss with attenuation values as low as 0.2 dB/km and, more recently, 0.1 dB/km [17] at 1550 nm. It, thus, follows that QKD networks make use of the existing optical fiber infrastructure, for cost efficiency purposes, as well. However, the fiber-based QKD approach is limited by exponential photon loss over distances beyond a few hundred kilometers, making only one photon in each 10^{10} survive over 1000 km with 0.1 dB/km fiber losses (See Appendix A).

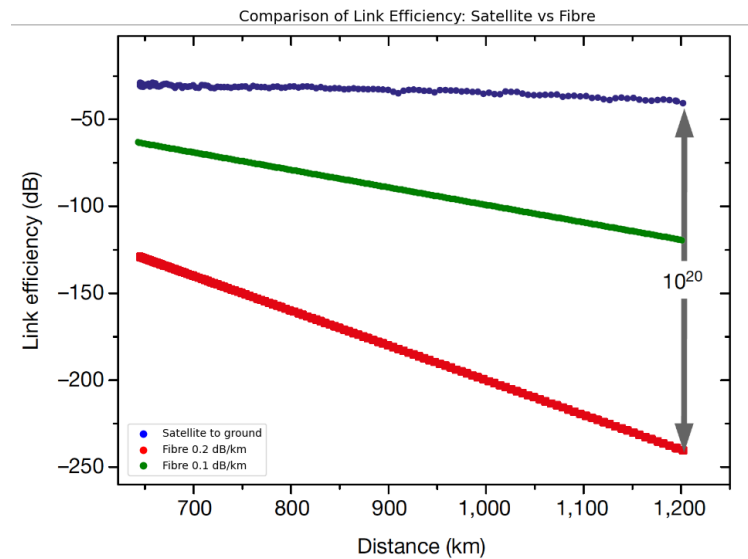


Figure 1: Link efficiencies for fiber-based and satellite-based transmissions over 645 – 1200 km. The red points correspond to 0.2 dB/km fiber loss while the blue points show satellite-to-ground measurements, both from [14]. The green points, corresponding to 0.1 dB/km fiber loss, were calculated and added here to reflect the recent advances in optical fibers reported in [17].

Although conceptually similar, satellite-based quantum communication offers a reasonable alternative for fiber-based networks, where photons are transmitted in free space between satellites and terrestrial stations with telescopes on both ends [8]. Experiments with the *Micius* satellite [16] have shown that satellite-to-ground channels can outperform optical fibers by more than twenty orders of magnitude in terms of achievable transmittance over thousand-kilometer scales. Fig. 1 shows that, unlike fibers, satellite channels maintain a robust link efficiency over long distances. Even with the recent improvement in fiber attenuation, the satellite-based approach has an advantage of several orders of magnitude, which highlights its essential

role in global deployments.

Atmospheric propagation, however, introduces challenges for Free Space Optical Quantum Communication (FSOQC), where photons are used as fragile information carriers and strongly affected by turbulence, scattering, absorption, scintillation, pointing errors, and wavefront aberrations. These effects cause fluctuations in transmittance, reduce link availability, and directly impact key QKD performance metrics, most importantly, the QBER and SKR [5]. Since secure and efficient quantum communication requires high transmittance and low error rates, it is important to understand and mitigate atmospheric effects to design robust free-space QKD systems.

This thesis studies and quantifies the impact of atmospheric effects on free-space QKD metrics, and link availability. It also proposes mitigation strategies at both the system and optical receiver levels. The adopted approach focuses on the downlink scenario with BB84 as the QKD protocol. Turbulence-informed theoretical models are combined with system-level optimization and receiver optical design to link physical atmospheric effects to practical system performance.

The manuscript is organized as follows. Chapter 2 introduces the geometric model of the downlink discussed here and the implemented QKD protocol. Chapter 3 dives deep into the atmospheric effects and the theoretical models for the different factors and their combined impact on QKD to set the scene for Chapter 4 which tackles system-level mitigation strategies, including wavelength selection and adaptive optics, parameterised based on Chapter 3. Further, Chapter 5 explores the optics of the ground receiver. The thesis concludes with a synthesis of the findings and outlook on satellite-based quantum communication.

2 Protocol and Geometry

2.1 The BB84 Protocol

BB84 is a prepare-and-measure QKD protocol based on encoding classical information into non-orthogonal quantum states, such that any eavesdropping attempt introduces detectable errors. First, Alice encodes classical bits into photon polarizations and transmits them over a quantum channel to Bob, who then measures each photon randomly in either the rectilinear or diagonal basis. When the basis choices match, they get correlated outcomes while mismatches mismatched bases randomize the results. Alice and Bob then confirm the measurement results over a public classical channel by announcing and reconciling the measurement bases. They keep the correctly measured photons to use as the key and discard the rest and then use some of the key bits to compute the QBER (which quantify the mismatch between their bits). Bob reveals some random bits and if the error rate exceeded the upper bound (typically $\sim 11\%$ for standard BB84 with one-way error correction), it corresponds with eavesdropping and the communication is considered insecure. Here lies the importance of addressing the atmospheric effects which compromise the security of the communication by increasing this mismatch, i.e. QBER, in downlinks.

2.2 Geometric Model of the Free-space QKD Downlink

A satellite-to-ground QKD downlink can be viewed as a free-space optical communication system consisting of three main elements: the transmitter on board the satellite, the propagation channel through the atmosphere, and the ground-based receiver. As we are considering satellite-based QKD link, the zenith angle changes as the satellite is moving in orbit, which changes the propagation path L in turn. The following expression for L is considered to account for these changes [7]:

$$L = \sqrt{(R_E + h)^2 + (R_E + h_0)^2(\cos^2 \zeta - 1)} - (R_E + h_0) \cos \zeta. \quad (1)$$

where $R_E \approx 6370$ km is Earth's radius.

At the satellite end, the transmitter generates a beam and directs it toward the Earth. The beam propagates over the slant distance L and diverges according to the rules of diffraction, so that its spot size increases with distance. The divergence effects are further magnified due to the atmospheric effects and pointing jitters which introduce more significant errors over the larger distances of satellite-based QKD. The ground receiver is equipped with a telescope of aperture radius a_R , which collects only the portion of the beam that falls within its opening. The fraction of collected power defines the efficiency of the link as will be shown in the next sections and this eventually affects the QBER.

3 Atmospheric Effects on Free-Space QKD

3.1 Attenuation

Attenuation is a major source of power loss in FSOC channels caused by the interaction of propagating photons with suspended particles such as aerosols, fog droplets, raindrops, and snowflakes. It introduces an exponential decay of the received optical signal, which reduces the link transmittance T over distance L as shown by the standard formula following Beer–Lambert law:

$$T = e^{-\gamma L}, \quad (2)$$

where γ is the attenuation coefficient combining the absorption and scattering coefficients of the particles in the atmosphere. Now, we make a distinction between the scattering and absorption contributions to attenuation to inform the wavelength selection.

3.1.1 Scattering

As the sizes of atmospheric particles are comparable to the wavelengths typically used, in the infrared region, *Mie scattering* provides the most accurate description of attenuation. In practical scenarios, weather conditions such as fog, haze, rain, or snow reduce the atmospheric visibility V , which directly governs the specific attenuation. For modeling purposes, the Kim model [11] is adopted, as it improves on the Kruse model and captures how low visibility scenarios are independent of wavelength based on empirical data. The scattering coefficient is thus:

$$\gamma = \left(\frac{3.91}{V} \right) \left(\frac{\lambda}{550} \right)^{-p}, \quad (3)$$

where V is the visibility in kilometers, λ the wavelength in nanometers, and

$$p = \begin{cases} 1.6 & \text{for } V > 50 \text{ km,} \\ 1.3 & \text{for } 6 \text{ km} \leq V \leq 50 \text{ km,} \\ 0.16V + 0.34 & \text{for } 1 \text{ km} \leq V < 6 \text{ km,} \\ V - 0.5 & \text{for } 0.5 \text{ km} \leq V < 1 \text{ km,} \\ 0 & \text{for } V < 0.5 \text{ km.} \end{cases}$$

3.1.2 Absorption

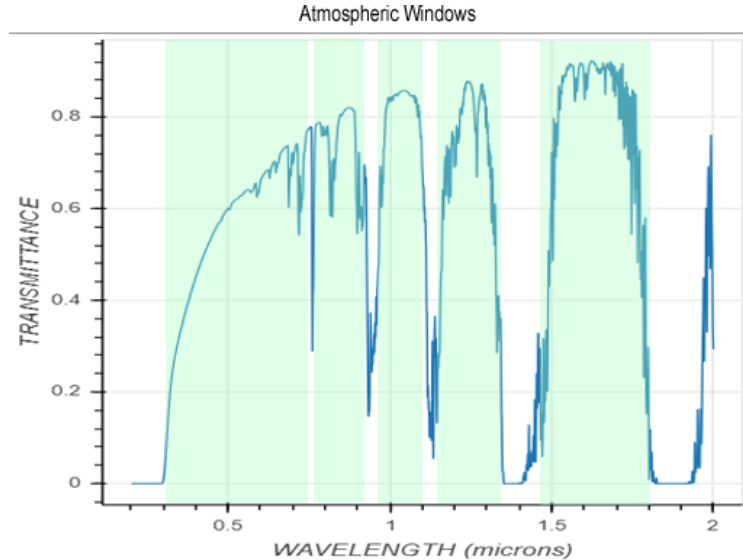


Figure 2: Atmospheric transmittance as a function of wavelength. Generated using MODTRAN Demo using the mid-latitude summer atmosphere model with urban aerosol model which accounts for absorption. Transmittance windows (wavelengths considered for free-space QKD) are highlighted in green.

The absorption coefficient can be defined as:

$$\alpha = \sigma N \quad \text{where } \sigma \text{ and } N \text{ are the effective cross section and the absorbent concentration} \quad (4)$$

Molecular absorption happens when the incident beam corresponds with the resonant frequency of gas molecules, mainly water vapor (H_2O), carbon dioxide (CO_2), and ozone (O_3). Fig. 2 shows that absorption occurs at discrete bands with some areas of the spectrum having effectively zero transmittance. The other areas are called *atmospheric windows* and represent the wavelength ranges where absorption is weak and

photons can propagate with relatively low loss. In these areas, absorption effect is negligible compared to turbulence and scattering effects [1].

To simplify the optimization work, selected wavelengths should be limited to these atmospheric windows accounting for the absorption effects. A specific wavelength can further be decided on using the scattering coefficient to calculate the transmittance due to weather conditions as follows:

$$\eta_{\text{weather}} = e^{-\gamma L}. \quad (5)$$

3.2 Beam wandering

Beam wandering is one of the most prominent turbulence-induced effects in FSO QKD links. It refers to the random displacement of the beam centroid around the intended line of sight as the optical wave propagates through turbulent layers of the atmosphere. Physically, this occurs because refractive index fluctuations—caused by temperature and wind velocity gradients—act as random prisms that locally bend the wavefront. As a result, the beam does not travel along a perfectly straight trajectory but instead “wanders” around the nominal optical axis. This random displacement of the beam centroid reduces the coupling efficiency, which is the proportion of the signal photons successfully channeled into the receiver aperture. This displacement can be described statistically as a Gaussian-distributed random variable with variance σ^2 [7] which is driven by two main factors:

(a) Pointing and tracking errors (σ_{pe}^2) caused by angular jitter and transmitter misalignment. For an angular misalignment with standard deviation θ_p over a propagation distance L , the corresponding beam displacement variance is:

$$\sigma_{\text{pe}}^2 = (L\theta_p)^2, \quad (6)$$

where $L\theta_p$ represents the standard deviation of lateral displacement at the receiver plane [2]. FSO links typically experience pointing jitter angles on the order of $\theta_p \approx 1 \mu\text{rad}$ [7] which gives:

$$\sigma_{\text{pe}}^2 \simeq 10^{-12} L^2, \quad (7)$$

(b) Turbulence-induced fluctuations (σ_{turb}^2), which result from random refractive index variations along the propagation path, typically modeled through the refractive index structure constant $C_n^2(h)$. These distortions are more elaborate, as they depend on the integrated turbulence strength along the link and contribute to beam wander and scintillation.

The total beam wander variance can thus be written as [7]:

$$\sigma^2 = \sigma_{\text{pe}}^2 + \sigma_{\text{turb}}^2. \quad (8)$$

The atmospheric turbulence strength is governed by the wind velocity profile. A widely used parameterisation is given by [9]:

$$v(h) = v_G + v_T \exp\left[-\left(\frac{h \cos(\zeta) - H_T}{L_T}\right)^2\right] [\sin^2 \phi + \cos^2 \phi \cos^2 \zeta]^{1/2}, \quad (9)$$

where v_G is the wind velocity at the ground level, v_T is the wind velocity at tropopause, ζ is the zenith angle of observation, H_T and L_T are the tropopause height and thickness, and ϕ is the wind direction relative to telescope azimuth, with h as the altitude.

This is substituted for into the improved model for the altitude-dependent refractive index structure constant given by [21] which accounts for the stronger turbulence near the surface during the day:

$$C_n^2(h) = M \left[1.04 \times 10^{-3} \left(\frac{9 \text{ m/s}}{v(h+h_g)} \right)^2 \left(\frac{h+h_g}{10^5 \text{ m}} \right)^{10} \exp\left(-\frac{h+h_g}{1200 \text{ m}}\right) + 2.7 \times 10^{-16} \exp\left(-\frac{h+h_g}{1700 \text{ m}}\right) \right] + C_n^2(h_0) \left(\frac{h_0}{h} \right)^{4/3} \quad (10)$$

where M and $C_n^2(h_0)$ are constants, h , h_g and h_0 are the altitude, the ground height above sea level and the instrument height above the ground level, respectively, and $v(h+h_g)$ is the wind velocity profile obtained from Eq. (9).

This $C_n^2(h)$ model connects meteorological conditions with the turbulence-induced beam wander term σ_{turb}^2 as follows [7]:

$$\sigma_{\text{tb}}^2 = 7.25 C_n^2 w_0^{-\frac{1}{3}} L^3 \int_0^1 d\xi \xi^2 \left[\frac{1}{f^{1/6}(\xi)} - \frac{\kappa_0^{1/3} w_0^{1/3}}{\left[1 + \kappa_0^2 w_0^2 f(\xi) \right]^{1/6}} \right], \quad (11)$$

where w_0 is the initial beam waist, $\kappa_0 = 2\pi/L_0$ and $L_0 \approx 1-100 \text{ m}$ which is the outer scale of turbulence, i.e. the largest size of swirling air motions (eddies) in the atmosphere beyond which the air flow is too smooth to distort an optical beam.

As the goal is to evaluate the beam displacement directly at the receiver's end where it impacts the coupling efficiency (the proportion of the signal photons successfully channeled into the receiver's fiber or detector), the expressions are defined accordingly below in terms of the beam parameters at the *receiver plane*, rather than at the transmitter:

$$f(\xi) = [\Omega + (1 - \Omega)\xi]^2 + 1.63 (\sigma_{\text{Ry}}^2)^{6/5} \Lambda (1 - \xi)^{16/5}, \quad (12)$$

where the beam parameters at the receiver are defined as

$$\Omega = 1 + \frac{L}{R_L}, \quad \Lambda = \frac{2L}{kw_L^2}, \quad (13)$$

with the optical wavenumber $k = 2\pi/\lambda$ and R_L the radius of curvature which naturally increases due to diffraction as the beam propagates in free space over L distance. It can be defined as follows[2]:

$$R(L) = L \left[1 + \left(\frac{\pi w_0^2}{L\lambda} \right)^2 \right] \quad (14)$$

while w_L is the beam radius at the receiver plane as defined in Eq. 16. The turbulence strength is quantified in Eq. 12 by the Rytov variance:

$$\sigma_{\text{Ry}}^2 = 1.23 C_n^2 k^{7/6} L^{11/6}, \quad (15)$$

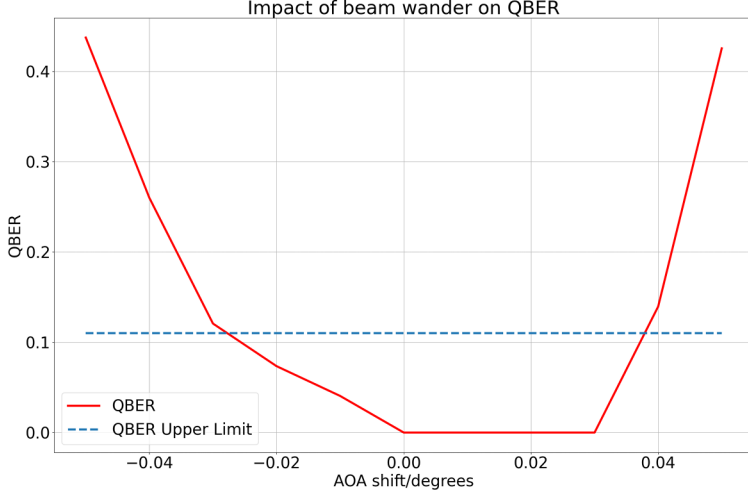


Figure 3: Beam wander modeled as AoA shifts over a 20m link increases QBER beyond the security limit

which reflects the dependence on the refractive index structure parameter C_n^2 .

We used the angle of arrival (AoA), which capture how the incoming wave temporarily deviates from its intended path, approximated by the source rotation angle [4], to model beam wander in a simulation of a BB84 receiver. Upon rotating the source, spot diagrams showed power leakage into the wrong detectors, which caused an increase in QBER. Fig. 3 shows that over a 20 m free-space link, angular deviations beyond $\pm 0.03^\circ$ push the QBER beyond the 0.11 security limit. As σ_{pe} scales linearly with the link length, these deviations have more significant effects in satellite-based QKD.

3.3 Beam broadening

Diffraction also causes the light beam to spread continuously. This is expressed in the broadened beam radius as follows [13]:

$$w(L) = w_0 \sqrt{1 + \left(\frac{L\lambda}{\pi w_0^2} \right)^2}, \quad (16)$$

This formulation, however, accounts only for beam divergence due to diffraction. In addition to beam wandering, turbulence also contributes to the beam spread, which increases the spot size at the receiver and further reduces coupling efficiency. The long-term beam radius in the presence of turbulence is described by [7]:

$$w_{lt} = w_L \sqrt{1 + 1.63(\sigma_{Ry}^2)^{6/5}\Lambda}, \quad (17)$$

which depends explicitly on the Rytov variance σ_{Ry}^2 , and therefore on the turbulence strength. Thus, it can be directly used to estimate turbulence-induced losses by plugging it into the long-term coupling efficiency into a receiver aperture with radius a_R as follows [7]:

$$\eta_{lt} = 1 - e^{-\frac{2a_R^2}{w_{lt}^2}}. \quad (18)$$

The same formula can be used to get η_{coupling} , which accounts for fiber-coupling efficiency, in which case a_R will be the fiber core radius and w will be the beam radius at the collection aperture at the fiber-coupling plane [6]. Now, the total link transmittance can be expressed as the product of all contributing factors:

$$\eta_{\text{tot}} = \eta_{\text{weather}} \eta_{\text{lt}} \eta_{\text{eff}}, \quad (19)$$

where η_{weather} accounts for absorption and scattering, η_{lt} for turbulence-induced broadening, and η_{eff} for the receiver's detection efficiency, which can be further decomposed as:

$$\eta_{\text{eff}} = \eta_t \eta_{\text{optics}} \eta_{\text{coupling}} \eta_{\text{QE}}, \quad (20)$$

where η_{QE} is the quantum efficiency of the detector and η_t is the telescope transmission efficiency expressed as:

$$\eta_t = \frac{2}{\alpha^2} \left(e^{-\alpha^2} - e^{-\alpha^2 \Xi^2} \right)^2, \quad (21)$$

with $\alpha = a_R/w_{LT}$ the ratio of telescope aperture radius to the Gaussian beam radius, and $\Xi = b/a_R$ is the ratio of the secondary radius b [12].

η_{optics} represents transmission losses from optical elements such as mirrors and lenses as follows:

$$\eta_{\text{optics}} = \prod_{i=1}^N T_i, \quad (22)$$

where T_i is the transmittance (or reflectivity) coefficient of the i -th optical surface, and N is the total number of surfaces in the receiver.

η_{coupling} can be expressed as follows [10]:

$$\eta_{\text{coupling}} = S(\%) \times 0.74 + 1.84 \quad (23)$$

where S is the Strehl ratio, which quantifies the degradation of image quality due to atmospheric turbulence in the absence of wavefront correction and is expressed as follows [13]:

$$S = \left[1 + \left(\frac{2a_R}{r_0} \right)^{5/3} \right]^{-6/5} \quad (24)$$

where r_0 is the Fried parameter defined in later sections.

3.4 Scintillation

In addition to beam wandering and beam broadening, atmospheric turbulence also produces random fluctuations in the received optical intensity, known as *scintillation*. It is caused by small- and medium-scale refractive index fluctuations that act as random lenses, locally focusing and defocusing the propagating beam. Scintillation strength is quantified by the *scintillation index*. For satellite downlinks, where the refractive index structure parameter C_n^2 varies with altitude and the propagation occurs at a finite zenith angle ζ , it is

defined by [7]:

$$\sigma_I^2(h, \zeta) = \exp \left[\frac{0.49 \sigma_{Ry}^2(h, \zeta)}{\left(1 + 1.11 \sigma_{Ry}^{12/5}(h, \zeta)\right)^{7/6}} + \frac{0.51 \sigma_{Ry}^2(h, \zeta)}{\left(1 + 0.69 \sigma_{Ry}^{12/5}(h, \zeta)\right)^{5/6}} \right] - 1, \quad (25)$$

Here, a variation of Rytov variance depending on altitude and zenith is given by:

$$\sigma_{Ry}^2(h, \zeta) = 2.25 \left(\frac{2\pi}{\lambda} \right)^{7/6} \sec^{11/6}(\zeta) \int_{h_0}^h (h' - h_0)^{5/6} C_n^2(h') dh'. \quad (26)$$

with h the (satellite) altitude, h_0 is the ground station altitude, and $C_n^2(h')$ is the altitude-dependent refractive index structure parameter from Eq.(10).

Scintillation leads to the received signal fading quickly. However, it has minimal impact on our scenario, where BB84 is implemented over a downlink [19]. Thus, it is not considered in the proposed mitigation.

3.5 Wavefront Aberrations

The random refractive index fluctuations caused by turbulence distort the phase front of an optical wave as it propagates through the atmosphere. The distortions are characterized by the following parameters [9]:

(a) The Fried parameter r_0 quantifies the strength of atmospheric turbulence along the line of sight and represents the transverse coherence length of the optical wavefront. It can be pictured as the diameter of a calm area in the turbulent atmosphere where the optical field remains coherent and only affected by diffraction rather than turbulence. It is defined for downlink as follows [20]:

$$r_0 = \left[0.423 \left(\frac{2\pi}{\lambda} \right)^2 (\sec \zeta) \int_{h_0}^h C_n^2(h') dh' \right]^{-3/5} \quad (27)$$

r_0 sets a limit when exceeded by the telescope aperture diameter D_R , which is the case for available telescopes, turbulence limits the resolution of the telescope. Here comes the role of adaptive optics which take into account the Fried parameter.

(b) The isoplanatic angle θ_0 can be described as the angular separation over which the turbulence-induced phase distortions remain correlated. It is given by:

$$\theta_0 = \left[2.914 \left(\frac{2\pi}{\lambda} \right)^2 (\sec \zeta)^{8/3} \int_{h_0}^h C_n^2(h') h'^{5/3} dh' \right]^{-3/5} \quad (28)$$

In BB84 downlink, the turbulence distortions are measured using a beacon, and the resulting correction is applied across the ground telescope aperture. For this correction to also be valid for the quantum signal, the angular separation between the beacon and the quantum beam, as observed from the ground, must be smaller than θ_0 , otherwise the beacon and the quantum signal traverse different turbulence columns and experience uncorrelated distortions, in which case the beacon-based correction cannot correct for the actual signal wavefront.

(c) The coherence time τ_0 can similarly be expressed as the time interval over which the turbulence-induced phase distortions remain correlated, and is given by:

$$\tau_0 = 0.314(\cos \zeta) \frac{r_0}{v_0}, \quad (29)$$

where v_0 is the effective wind velocity, determined by a weighted average of the wind velocity profile from Eq. (9) as follows:

$$v_0 = \left[\frac{\int_{h_0}^h C_n^2(h') v(h')^{5/3} dh'}{\int_{h_0}^h C_n^2(h') dh'} \right]^{3/5}. \quad (30)$$

While θ_0 gives the spatial scale, τ_0 gives the temporal scale over which the corrections for distortions remain valid. The significance of these parameters lies in quantifying the severity of turbulence effects. A smaller r_0 indicates stronger turbulence and a higher level of phase aberrations, while a smaller τ_0 implies that the turbulence is rapidly varying, which makes adaptive optics compensation challenging.

3.6 Background Noise

Background noise also limits free-space QKD links, particularly in daylight conditions or when operating at low elevation angles. Background photons originating from the sky radiance are collected by the receiver and may lead to erroneous detection events and increase the QBER.

The mean number of background photons per detection mode in the downlink configuration can be expressed as [18]:

$$\bar{n}_B^{\text{down}} = \Gamma_R H_\lambda^{\text{sky}}, \quad (31)$$

where H_λ^{sky} is the spectral sky radiance, which shows that daylight communications are challenging due to the increasing background photons. Γ_R is the receiver collection factor and given by:

$$\Gamma_R = \Delta\lambda \Delta t \Omega_{\text{fov}} a_R^2, \quad (32)$$

where each term represents a physical property of the receiver. $\Delta\lambda$ is the optical filter bandwidth, which specifies the width of the slice of EM spectrum the receiver allows to pass. A narrower $\Delta\lambda$ reduces the acceptable wavelength range which consequently reduces the amount of unwanted background radiation. Δt is the detector integration time, i.e. the time window during which the detector is open to count photons. Shorter times limit the background photons captured. Ω_{fov} is the receiver field-of-view solid angle which determines the portion of the sky the receiver is sensitive to, which can be expressed following the turbulence-limited formulation in [13] as follows:

$$\Omega_{\text{fov}} = \pi \left(1.22 \frac{\lambda}{2a_R} \left[1 + \left(\frac{2a_R}{r_0} \right)^{5/3} \right]^{3/5} \right)^2 \quad (33)$$

A smaller field-of-view restricts background photons but also requires more precise pointing and tracking. A larger aperture increases the amount of signal photons gathered. Although this might improve the link performance, it proportionally increases the background photons collected. It is thus important to carefully select the optimal combination of these parameters so that they are not too small to receive the signal.

3.7 Impact on QKD metrics

3.7.1 Secret Key Rate

A lower bound for SKR for practical protocols is given by:

$$S \geq q \{ -Q_\mu f(E_\mu) H_2(E_\mu) + Q_1 [1 - H_2(e_1)] \}, \quad (34)$$

where $q = 1/2$ for BB84, $f(E_\mu)$ is the error correction efficiency, $H_2(x) = -x \log_2 x - (1-x) \log_2(1-x)$ is the binary entropy function, Q_1 and e_1 are the detection probability and error rate of the single photon states, while Q_μ and E_μ are the overall detection and error rate (QBER), with [15]

$$Q_1 = \mu \eta_{\text{tot}} e^{-\mu}, \quad E_\mu \approx e_1 \quad (35)$$

where the mean photon number is $\mu = \frac{P_t \lambda}{hc f_t}$, P_t and f_t is the transmitter power and pulse rate. It should be noted, however, that attenuated laser sources are used in QKD to suppress multiphoton pulses which is prone to photon-number-splitting attack.

Here, we express SKR, assuming $f_e = 1$ (ideally), as follows:

$$R \geq q \{ -p_{\text{det}} H_2(QBER) + \mu \eta_{\text{tot}} e^{-\mu} [1 - H_2(QBER)] \}, \quad (36)$$

where p_{det} is the total detection probability per pulse and Q is QBER.

3.7.2 Detection Probability

The total detection probability can be obtained here by summing the contributions from the signal, background, and dark counts as follows:

$$p_{\text{det}} = p_{\text{sig}} + p_{\text{bg}} + p_{\text{dark}}. \quad (37)$$

Where $p_{\text{bg}} = \bar{n}_B$, and $p_{\text{dark}} = DCR \times \Delta t$ is the false counts registered by the detector due to its intrinsic dark count rate (DCR).

$$p_{\text{sig}} = \mu \eta_{\text{tot}} \quad (38)$$

3.7.3 Quantum Bit Error Rate (QBER)

The QBER is the ratio of the number of incorrectly detected bits to the total detected bits. Here, we define it using the contributions of signal and noise counts as follows:

$$Q = \frac{e_{\text{det}} p_{\text{sig}} + \frac{1}{2} (p_{\text{bg}} + p_{\text{dark}})}{p_{\text{det}}}. \quad (39)$$

As p_{bg} and p_{dark} are random, there is a 50% chance they are wrong. e_{det} is the erroneous detections (wrong detector clicks) due to system imperfections.

Thus, the secret key rate in Eq. (36) can be computed directly from the atmospheric channel transmittance, the background noise, and the detector noise parameters. This formulation explicitly links atmospheric effects and noise to QKD system performance and sets the stage for the mitigation strategies presented in the following section.

4 System-Level Mitigation Strategies

Building on the equations covered in the previous chapter, we analyze and present comparative optimization studies for key system parameters in the following subsections. It should be noted that the interpretation of the numerical results presented here focuses primarily on the qualitative trends across scenarios, which remain consistent with theoretical expectations.

4.1 Wavelength Selection

The choice of the wavelength is an important operational factor for free-space QKD as it affects channel attenuation, turbulence-induced distortions, and receiver performance as shown in the theoretical framework.

Here, we evaluate the impact of wavelength selection under different conditions. We first consider a bad weather scenario with reduced visibility and strong turbulence. The visibility is set to $V = 0.5$ km, representing dense fog, while the initial beam waist is taken in the typical range as $w_0 = 5$ cm. The turbulence ground-level structure constant is taken as $C_n^2(h_0) = 10^{-12} \text{ m}^{-2/3}$ at an instrument height of $h_0 = 10$ m, and the satellite is assumed at an altitude of $h = 300$ km with a zenith angle of $\zeta = 30^\circ$. The wind profile is characterized by a surface wind speed of $v_G = 10$ m/s and a maximum tropopause contribution of $v_T = 30$ m/s centered at $H_T = 10$ km with a scale thickness $L_T = 1$ km, while the azimuth angle is set to $\phi = 90^\circ$. Turbulence scaling is further adjusted with a ground offset $h_g = 100$ m and a multiplicative factor $M = 10$, assuming an outer scale $L_0 = 50$ m, consistent with typical atmospheric ranges of 1–100 m. Table 1 summarizes the results of a comparison study between wavelength candidates showing their effect on key atmospheric parameters that govern the link performance.

To represent clear weather with weak turbulence, visibility is increased to $V = 23$ km, corresponding to clear atmospheric conditions. The turbulence strength constant is set to $C_n^2(h_0) = 10^{-17} \text{ m}^{-2/3}$. For the wind profile, the surface wind speed is decreased to $v_G = 5$ m/s, while the maximum tropopause contribution is set to $v_T = 20$ m/s, representing calmer conditions. Table 2 shows the result of the comparison in better

Table 1: Wavelength performance under low visibility, strong turbulence, and windy weather conditions ($h_0 = 10$ m, $w_0 = 0.05$ m).

Parameter	810 nm	1064 nm	1550 nm	Best
γ	7.82×10^{-3}	7.82×10^{-3}	7.82×10^{-3}	–
$w(L)$ [m]	1.77	2.33	3.39	810 nm
σ_I^2	6.31×10^{-1}	7.06×10^{-1}	6.36×10^{-1}	810 nm
σ_{tb}^2 [m ²]	1.02×10^{-3}	1.02×10^{-3}	1.03×10^{-3}	–
w_{LT} [m]	1.83	2.37	3.42	810 nm
r_0 [m]	1.83×10^{-2}	2.53×10^{-2}	3.98×10^{-2}	1550 nm
θ_0 [rad]	4.05×10^{-6}	5.61×10^{-6}	8.82×10^{-6}	1550 nm
τ_0 [s]	4.96×10^{-4}	6.88×10^{-4}	1.08×10^{-3}	1550 nm

weather conditions.

Table 2: Wavelength performance under clear, calm weather and weak turbulence conditions ($h_0 = 10$ m, $w_0 = 0.05$ m).

Parameter	810 nm	1064 nm	1550 nm	Best
γ	1.03×10^{-4}	7.21×10^{-5}	4.42×10^{-5}	1550 nm
$w(L)$ [m]	1.77	2.33	3.39	810 nm
σ_I^2	1.76×10^{-1}	1.26×10^{-1}	8.00×10^{-2}	1550 nm
σ_{tb}^2 [m ²]	2.39×10^{-4}	2.39×10^{-4}	2.39×10^{-4}	–
w_{LT} [m]	1.79	2.33	3.40	810 nm
r_0 [m]	1.78×10^{-1}	2.46×10^{-1}	3.87×10^{-1}	1550 nm
θ_0 [rad]	1.08×10^{-5}	1.50×10^{-5}	2.36×10^{-5}	1550 nm
τ_0 [s]	9.44×10^{-3}	1.31×10^{-2}	2.06×10^{-2}	1550 nm

The above results indicate that 1550 nm and 810 nm could be the best wavelength candidates. While 810 nm offers lower beam spread, the 1550 nm wavelength provides better coherence parameters (r_0 , θ_0 , and τ_0). Eye safety is also a key consideration since laser beams are transmitted through open air and may inadvertently expose humans. The so-called “eye-safe” wavelengths are in the range of 1400-1800 nm; thus, 1550 nm have an advantage. Another aspect to consider is the radiance, which drops at higher wavelengths as shown in Fig. 4. This makes $\lambda = 1550$ nm a promising candidate for daytime QKD to reduce background noise which scales linearly with the radiance as shown in the previous chapter.

Among all performance metrics, the attenuation coefficient γ is the most critical in QKD scenario, as it directly governs channel loss and thus the secure key rate. In low-visibility conditions, the attenuation coefficients at the three candidate wavelengths are nearly identical, which confirms the earlier findings in [11]. A more decisive comparison can be made by looking the total transmittance. Fig. 5 shows that in clear weather conditions, the choice of $\lambda = 1550$ nm can double the transmittance.

4.2 Beam Waist Optimization

The beam waist w_0 is a fundamental parameter in Gaussian beam optics. It determines the initial spot size at the transmitter and affects beam divergence and wander directly. As shown in Chapter 1, the governing

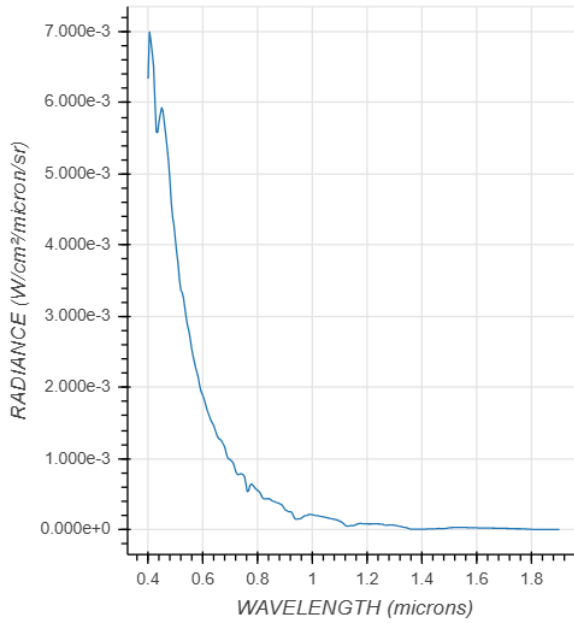


Figure 4: Spectral radiance of the daytime sky as a function of wavelength. Radiance is highest in the visible band ($\approx 0.4\text{--}0.6 \mu\text{m}$) and decreases sharply toward the near-infrared with minimal values beyond $1 \mu\text{m}$.

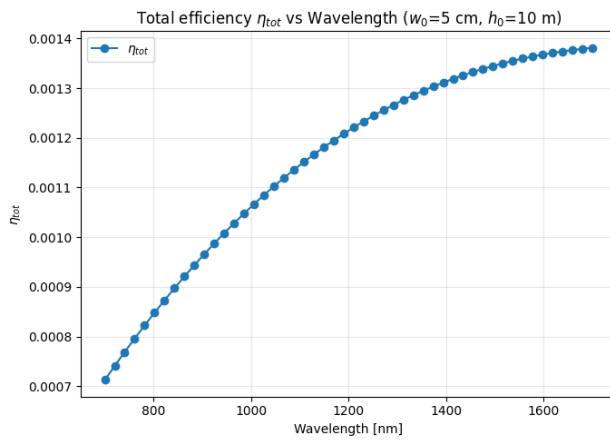


Figure 5: Total transmittance η_{tot} for different wavelengths under clear weather conditions

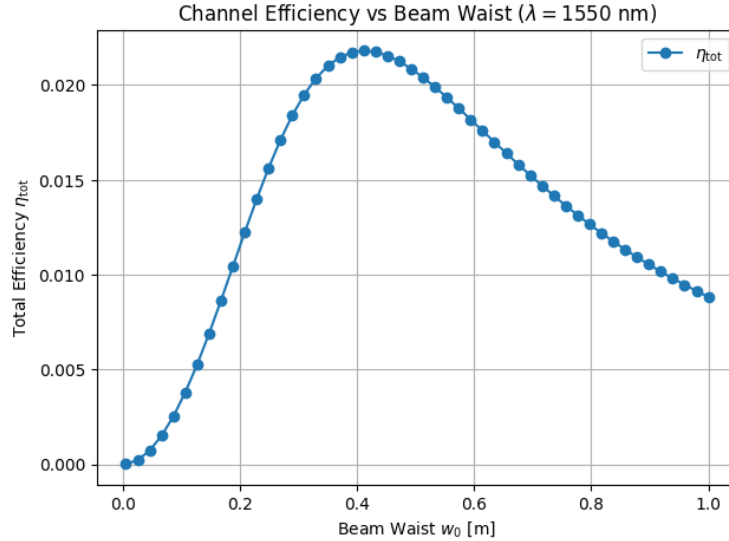


Figure 6: Total transmittance η_{tot} for different beam waist values w_0 at $\lambda = 1550$ nm. An optimum appears under the given parameters near $w_0 \approx 40$ cm, beyond which efficiency declines due to coupling mismatch. Such a large waist, however, is impractical for realistic QKD receivers, and smaller values (on the order of a few centimeters) provide a more practical trade-off between propagation robustness and coupling efficiency.

equations for the far-field beam radius $w(L)$, the turbulence-induced beam wander variance σ_{tb}^2 , and the long-term beam spot size w_{LT} depend on w_0 . Here, we carry out a comparison between three candidate values of w_0 chosen across the typical operating range (5 mm, 5 cm, and 10 cm), under the same set of atmospheric and system parameters used for the wavelength selection, with λ fixed at the winning value of 1550 nm as concluded in the previous section. Tables 3 and 4 summarize the results.

Table 3: Beam waist effect on selected parameters under low visibility, strong turbulence, and windy weather conditions.

Parameter	$w_0 = 5$ mm	$w_0 = 5$ cm	$w_0 = 10$ cm	Best
$w(L)$ [m]	33.9	3.39	1.70	10 cm
σ_{tb}^2 [m ²]	2.45×10^{-3}	1.03×10^{-3}	7.68×10^{-4}	10 cm
w_{LT} [m]	33.9	3.42	1.75	10 cm

Table 4: Beam waist effect on selected parameters under clear weather conditions.

Parameter	$w_0 = 5$ mm	$w_0 = 5$ cm	$w_0 = 10$ cm	Best
$w(L)$ [m]	33.9	3.39	1.70	10 cm
σ_{tb}^2 [m ²]	5.69×10^{-4}	2.39×10^{-4}	1.80×10^{-4}	10 cm
w_{LT} [m]	33.9	3.40	1.70	10 cm

The results clearly show that increasing the beam waist w_0 reduces both the long-term beam radius w_{LT} and the turbulence-induced beam wander variance σ_{tb}^2 , which could suggest that larger initial waists provide better robustness against diffraction and turbulence. This might imply that simply maximizing w_0 is always beneficial, particularly as increasing from 5 mm to 10 cm improved the link transmittance as shown in Fig.

6. However, this cannot be the case in practice as excessively large waists introduce significant coupling difficulties at the receiver. There is an upper bound for w_0 , beyond which the overall system efficiency drops. The figure shows how the coupling efficiency decreases once the waist becomes too large which confirms the trade-off between propagation robustness and receiver compatibility.

4.3 Ground Instrument Altitude h_0

The parameter h_0 represents the altitude of the ground instrument above the surface level, such as positioning the optical receiver on a rooftop or tower rather than at ground level. The choice of h_0 is relevant because the near-ground atmospheric layer is often the most turbulent and most affected by aerosols, fog, and local temperature gradients. Increasing h_0 might therefore reduce the impact of these near-surface disturbances. On the other hand, higher positions may also expose the link to stronger winds and layers with more variable turbulence. This makes the effect of h_0 dependent on weather conditions. To evaluate it, Tables 5 and 6 compare key turbulence parameters under both foggy turbulent conditions and clear weather for different h_0 .

Table 5: Ground instrument altitude effect under foggy turbulent conditions at $\lambda = 1550$ nm, $w_0 = 10$ cm.

Parameter	$h_0 = 0$ m	$h_0 = 10$ m	$h_0 = 20$ m	Best
σ_I^2	4.28×10^{-2}	6.36×10^{-1}	5.90×10^{-1}	0 m
σ_{tb}^2	6.08×10^{-5}	7.68×10^{-4}	1.82×10^{-3}	0 m
w_{LT} [m]	1.70	1.75	1.83	0 m
r_0 [m]	4.47×10^{-1}	3.98×10^{-2}	2.65×10^{-2}	0 m
θ_0 [rad]	4.02×10^{-5}	8.82×10^{-6}	5.22×10^{-6}	0 m
τ_0 [s]	1.21×10^{-2}	1.08×10^{-3}	7.21×10^{-4}	0 m

Table 6: Ground instrument altitude effect under clear weather conditions.

Parameter	$h_0 = 0$ m	$h_0 = 10$ m	$h_0 = 20$ m	Best
σ_I^2	8.02×10^{-2}	8.00×10^{-2}	7.98×10^{-2}	20 m
σ_{tb}^2	1.80×10^{-4}	1.80×10^{-4}	1.79×10^{-4}	20 m
w_{LT} [m]	1.70	1.70	1.70	–
r_0 [m]	3.86×10^{-1}	3.87×10^{-1}	3.88×10^{-1}	20 m
θ_0 [rad]	2.36×10^{-5}	2.36×10^{-5}	2.36×10^{-5}	–
τ_0 [s]	2.05×10^{-2}	2.06×10^{-2}	2.06×10^{-2}	–

It can be concluded that the effect of h_0 is minimal, with only slight improvements in some parameters at higher altitudes under clear weather conditions. However, under foggy turbulent conditions, the performance degrades with altitude. This suggests that in clear air, higher receiver altitude gives only minor gains, while in foggy conditions lower altitudes provide more stability. The isoplanatic angle θ_0 stays nearly constant in clear air, but drops quickly with altitude in fog because of near-ground turbulence. We also calculate η_{tot} for the examined altitudes, and the results show that the total efficiency exhibits a generally smooth dependence on h_0 with some variations. As illustrated in Fig. 7, the efficiency tends to increase with altitude.

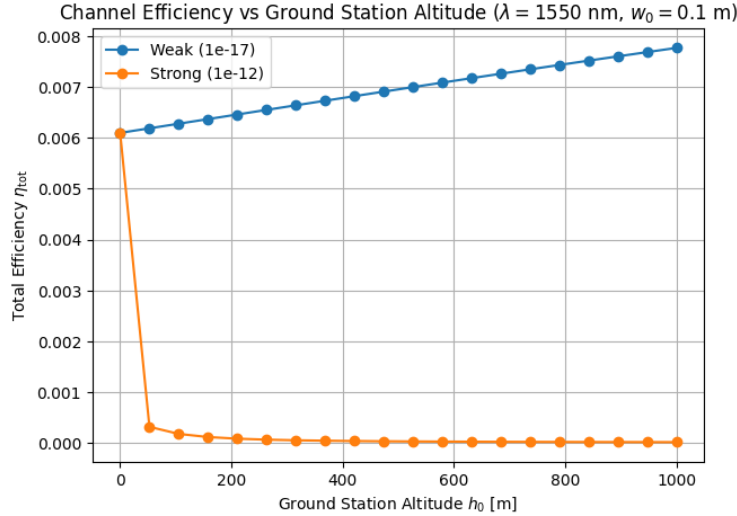


Figure 7: Total channel efficiency η_{tot} as a function of ground instrument altitude h_0 at $\lambda = 1550$ nm and $w_0 = 0.1$ m. The curve shows a minimal increase of efficiency with altitude in weak turbulence while the efficiency drops with altitude in strong turbulence.

4.4 Receiver Aperture Radius a_R

The receiver aperture radius a_R is a trade-off as a larger aperture captures more of the beam and reduces signal loss once $a_R > w_{LT}$, but it also admits more background photons and turbulence effects.

Table 7: Receiver telescope aperture candidates a_R and corresponding link parameters under foggy, windy, and turbulent weather.

Parameter	$a_R = 0.10$ m	$a_R = 0.20$ m	$a_R = 0.50$ m	Best
η_{lt}	5.80×10^{-3}	2.30×10^{-2}	1.33×10^{-1}	0.50 m
$\langle \beta_a^2 \rangle$	1.54×10^{-10}	1.23×10^{-10}	9.03×10^{-11}	0.50 m
Ω_{fov}	7.68×10^{-9}	7.28×10^{-9}	7.13×10^{-9}	0.50 m
Γ_R	1.88	7.13	43.7	0.10 m
n_B^{down}	1.88×10^{-6}	7.13×10^{-6}	4.37×10^{-5}	0.10 m
S	4.55×10^{-2}	2.55×10^{-2}	1.96×10^{-2}	0.10 m

Table 8: Receiver telescope aperture candidates a_R and corresponding link parameters under clear weather.

Parameter	$a_R = 0.10$ m	$a_R = 0.20$ m	$a_R = 0.50$ m	Best
η_{lt}	6.11×10^{-3}	2.41×10^{-2}	1.39×10^{-1}	0.50 m
$\langle \beta_a^2 \rangle$	3.49×10^{-12}	2.77×10^{-12}	2.04×10^{-12}	0.50 m
Ω_{fov}	3.97×10^{-10}	1.67×10^{-10}	9.39×10^{-11}	0.50 m
Γ_R	9.71×10^{-2}	1.64×10^{-1}	5.75×10^{-1}	0.10 m
n_B^{down}	9.71×10^{-8}	1.64×10^{-7}	5.75×10^{-7}	0.10 m
S	5.43×10^{-1}	3.30×10^{-1}	1.07×10^{-1}	0.10 m

In practice, however, receivers often use telescopes with a central obscuration due to the secondary mirror, which affects the aperture efficiency as expressed in Eq. (21). Here, we carry out a comparison between typical aperture radius candidates. The background noise parameters are selected to represent realistic receiver operating conditions. A spectral filter bandwidth of $\Delta\lambda = 1 \text{ nm}$ is assumed, which corresponds to a narrow-band optical filter that passes the signal wavelength used in QKD and blocks other wavelengths. The detector integration time is set to $\Delta t = 1 \text{ ns}$. The background spectral radiance is modeled as $H_{\text{sky}} \approx 10^{-6} \text{ W m}^{-2} \text{ nm}^{-1} \text{ sr}^{-1}$, for clear-sky night-time conditions that ensures more robustness even under moderate increases in sky brightness. Finally, the secondary mirror radius is taken as $b = 1/3 \times aR \text{ m}$, corresponding to a typical obscuration in Schmidt–Cassegrain telescopes of $\approx 30\%$ of the primary aperture diameter.

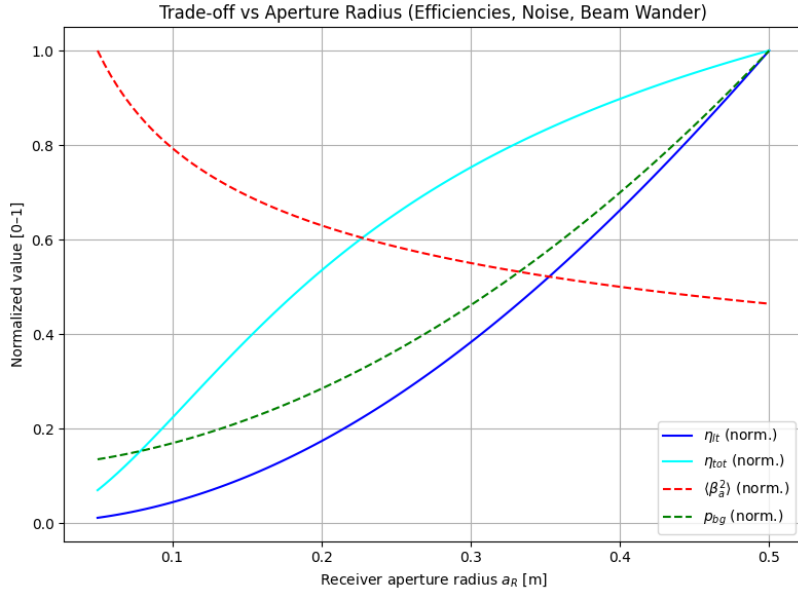


Figure 8: Trade-off between receiver aperture radius a_R and link parameters, showing collection efficiency, angular variance, and background noise in clear weather. An optimal range appears around $a_R \approx 0.3 \text{ m}$.

η_{lt} rises consistently with increasing aperture radius from 0.10 to 0.50 m, which reflects larger portion of the Gaussian beam admitted through the aperture using this variation of Eq. (18) to account for the secondary mirror:

$$\eta_{lt,SCT} = e^{-\frac{2b^2}{w_{lt}^2}} - e^{-\frac{2a_R^2}{w_{lt}^2}}. \quad (40)$$

In addition, the aperture radius directly influences the angle-of-arrival variance, given by:

$$\langle \beta_a^2 \rangle = 2.91 \sec(\zeta) \left(\int_{h_0}^H C_n^2(h) dh \right) D_R^{-1/3}, \quad D_R = 2a_R, \quad (41)$$

where increasing a_R reduces AoA fluctuations, which improves pointing stability and reduces turbulence-induced coupling losses.

On the other hand, although Ω_{fov} decreases slightly with aperture size in the reported results, the effective background collection factor Γ_R still increases with a_R because of the quadratic dependence on aperture

area. Thus, larger apertures inevitably capture more background photons and result in more noise which can deteriorate the QBER.

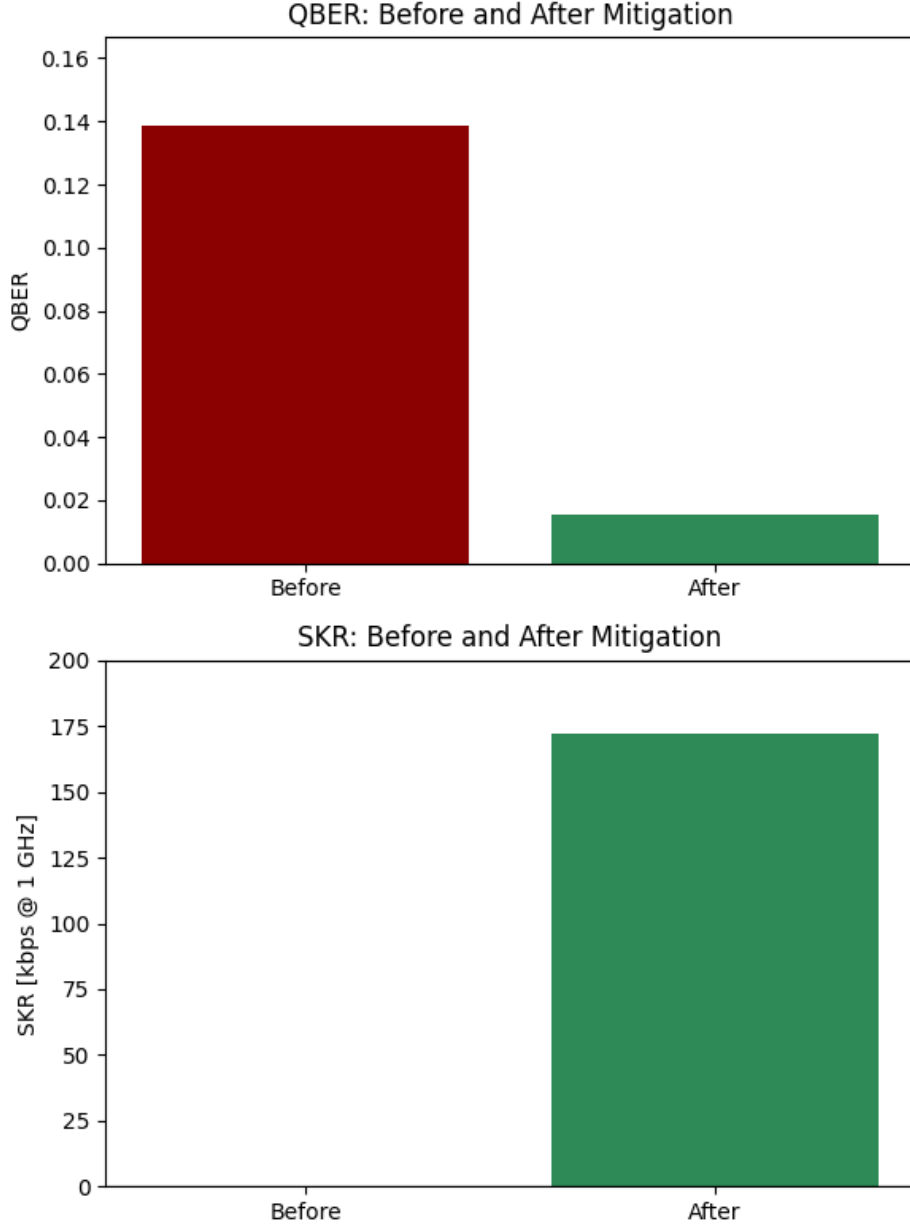


Figure 9: Comparison of QBER and SKR before and after applying operational mitigations. Without mitigation, $\text{QBER} \approx 14\%$ exceeds the BB84 security threshold ($\approx 11\%$), giving negligible SKR. After mitigation, QBER drops below 2% and SKR reaches ~ 170 kbps at a 1 GHz clock rate.

Therefore, the aperture radius a_R must balance three effects: larger apertures improve signal collection and turbulence resilience, but also increase background noise. For robust QKD operation, a moderate choice around 0.3 m could offer the best compromise as shown in Fig. 8 given that the results reported above are quite close for some parameters.

To illustrate the practical impact of the proposed mitigation strategies so far, Fig. 9 compares QBER and SKR before (using non-optimal values) and after mitigation (using the optimal values we found). It confirms the transition from an insecure channel, with QBER > %11 to one with a positive key rate.

4.5 Beam Wander and Focal Plane Displacement

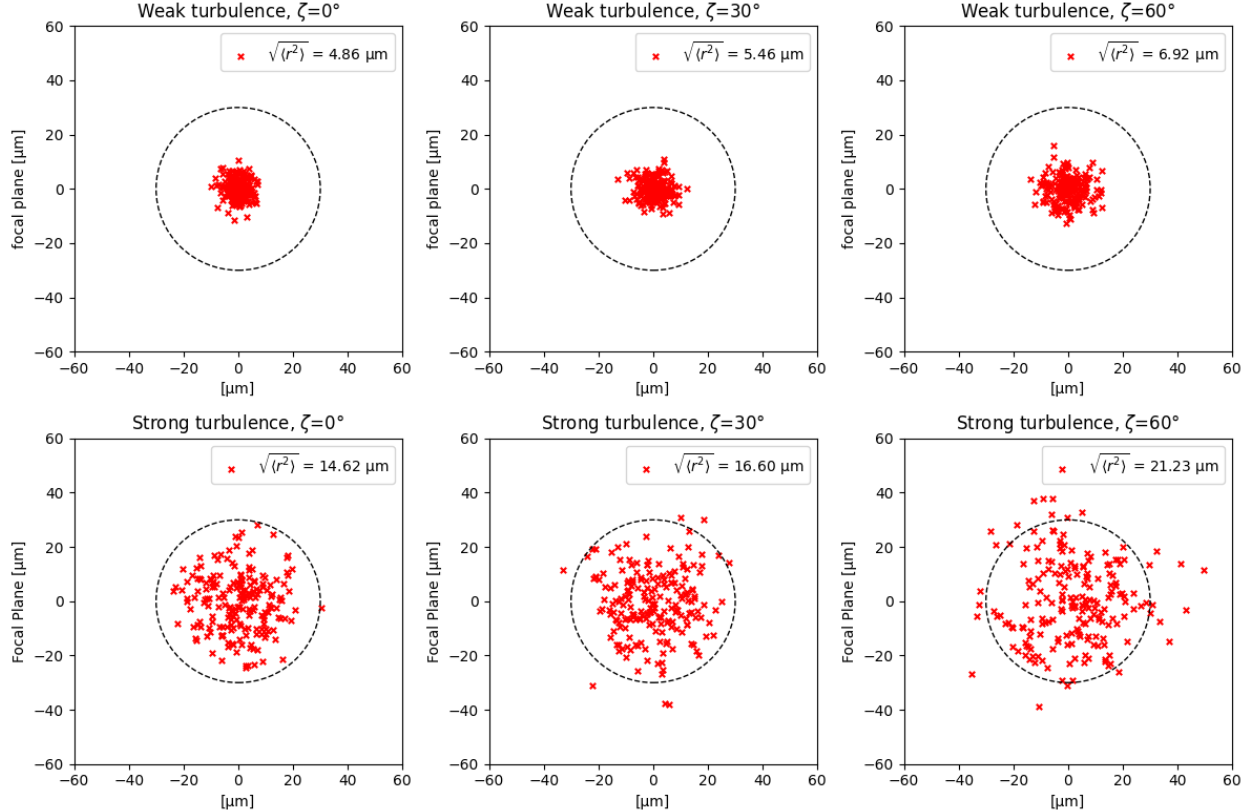


Figure 10: Monte Carlo simulation of beam wander at the focal plane for weak ($C_n^2(h_0) = 10^{-15}$) and strong ($C_n^2(h_0) = 10^{-13}$) turbulence conditions, at zenith angles of 0° , 30° , and 60° . Red crosses represent instantaneous spot centroids, while the dashed circle represents the detector radius ($30 \mu\text{m}$). Increased turbulence strength and zenith angle both enlarge the RMS displacement $\sqrt{\langle r_a^2 \rangle}$ which causes higher coupling losses.

As discussed in the previous chapter, turbulence-induced fluctuations in the angle of arrival can be quantified by the variance $\langle \beta_a^2 \rangle$ which translates into a displacement of the focal spot at the receiver plane. For a telescope with focal length f , the root-mean-square (RMS) displacement is expressed as

$$\sqrt{\langle r^2 \rangle} = f \tan\left(\sqrt{\langle \beta_a^2 \rangle}\right). \quad (42)$$

Eq. (42) highlights the dual role of optical design: a shorter focal length reduces the mapping of angular jitter into the focal plane, while a larger aperture reduces the jitter itself. Together, these relations demonstrate the trade-offs between aperture size, focal length, and turbulence-induced beam wander, which directly affect

coupling efficiency in free-space QKD receivers.

To illustrate this effect, Fig. 10 presents Monte Carlo simulations of beam centroid positions at the focal plane under weak and strong turbulence conditions for zenith angles of 0° , 30° , and 60° . The results confirm that both stronger turbulence and higher zenith angles increase the RMS displacement $\sqrt{\langle r_a^2 \rangle}$, which raises the probability of the focal spot wandering outside the detector active area. This directly reduces the effective coupling efficiency and, consequently, increases the QBER.

An additional method for mitigating beam wander is through the receiver's optical design. From Eq. (42), the focal plane displacement scales linearly with the focal length f . Hence, reducing the effective focal length decreases the mapping from angular jitter to spatial displacement, which improves spot stability at the detector. This does not eliminate turbulence effects but limits their impact on coupling efficiency. The trade-off is that a shorter focal length increases the acceptance angle and background photon collection. Thus, the effective focal length is determined by the optical configuration, which must be optimized in conjunction with parameters such as aperture size and field stops.

5 Receiver Optical Design

A typical receiver for BB84 QKD consists of three main subsystems: the telescope front-end, the optical filtering and coupling stage, and the single-photon detection module. The telescope collects the incoming free-space beam, suppresses aberrations, and focuses it onto the receiver plane. A classical beacon beam is often transmitted alongside the quantum signal as part of the acquisition, tracking, and pointing (ATP) system. At the receiver, a dichroic mirror separates the beacon from the quantum channel: the beacon is directed to a position-sensitive sensor, such as a quad cell, which drives a fast steering mirror for tip/tilt correction [4]. This ATP-assisted stage mitigates beam wander and corrects misalignment, which improves coupling efficiency. Meanwhile, the quantum signal passes through narrowband interference filters and field stops to eliminate background photons before coupling into a single-mode fiber or onto the detectors. Finally, the detection module performs basis selection (e.g., using polarizing beam splitters) and registers the quantum states encoded in the photon polarization.

The choice of receiver design parameters is guided by the system-level analysis of Chapter 4. The numerical simulations above showed that operation at $\lambda = 1550\text{ nm}$ offers the most turbulence tolerance and eye safety. For the transmitter, beam waists in the centimeter range are a practical compromise between divergence and sensitivity to pointing errors. On the receiver side, an aperture radius of $\approx 0.3\text{ m}$ captures most of the beam energy while avoiding excessive background collection. Also, a relatively short effective focal length reduces the mapping of angular jitter into focal plane displacement. These results set the parameter range for the Schmidt–Cassegrain telescope and the associated ATP-assisted coupling system described below.

5.1 Telescope

The receiver front-end uses a Schmidt–Cassegrain Telescope (SCT) (Fig. 11), which combines a spherical primary mirror, a convex secondary mirror, and a thin Schmidt corrector plate at the entrance aperture. The

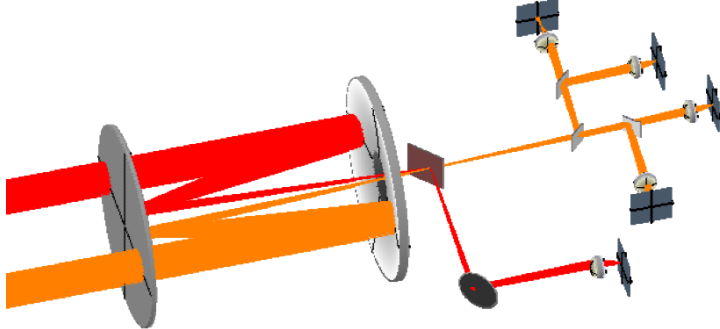


Figure 11: Ray-tracing layout of a SCT connected to a BB84 detection module. Incoming parallel rays are first corrected by the Schmidt plate (left), then reflected by the convex secondary mirror (center), and finally focused by the concave primary mirror (right) through the central aperture. The focused beam then passes to a dichroic mirror, which separates the quantum signal from the co-propagating beacon according to the wavelength.

corrector compensates for spherical aberration, allowing both mirrors to remain spherical and hence easier to fabricate. The optical path proceeds as follows: incoming rays first pass through the Schmidt corrector, which introduces a small aspheric deformation to cancel primary spherical aberration. The rays are then reflected by the large concave primary mirror toward the convex secondary mirror, which folds the optical path and increases the focal length. The light finally returns through a central aperture in the primary mirror to the focal plane, where a dichroic element can separate the quantum signal from a the ATP beacon beam.

5.2 Quadrant Detector

The quantum signals are typically detected by single photon detectors. The system can be improved by using a quadrant detector (QD) or quad-cell sensor to measure the instantaneous position of the focused spot via the beacon. This device is divided into four active regions, and by comparing the photocurrents from each quadrant, the centroid displacement of the beam relative to the optical axis can be determined. Quadrant detectors are particularly suited for tip/tilt correction because they provide high temporal resolution (tens of MHz bandwidth) and sub-micron spatial resolution [6].

5.3 Tip/Tilt Mirror

To actively correct wavefront tilt caused by atmospheric turbulence, the receiver incorporates a fast steering mirror (FSM) positioned before the focal plane. The FSM is controlled in closed-loop operation using the error signals generated by the quadrant detector [4]. In this scheme, the detector continuously senses AoA fluctuations, and the FSM compensates them by applying the corresponding tilt to the incoming beam, thereby stabilizing the centroid at the detector plane.

Tip/tilt correction addresses the dominant low-order aberration in turbulent channels (beam wander) and can reduce the standard deviation of focal spot displacement by more than 80% in both weak and strong turbulence regimes [20]. Although higher-order aberrations remain uncorrected, this process significantly reduces pointing error and enhances the effective coupling efficiency and forms the foundation of adaptive optics stabilization in free-space QKD links.

Conclusion

This thesis has examined the impacts of atmospheric propagation on free-space QKD using numerical simulations to provide a comparative study of the parameters in order to mitigate the effects at both the system and receiver levels. We began with BB84 protocol as the reference scheme with a geometric model of the satellite downlink channel. We then analyzed attenuation, turbulence-induced beam wander and broadening, scintillation, wavefront aberrations, and background noise theoretically. Each of these effects was linked explicitly to QKD performance metrics, particularly the QBER and the SKR.

Building on this theoretical framework, system-level mitigation strategies were explored, including wavelength selection, beam waist optimization, ground station altitude, and receiver aperture design. The results highlighted trade-offs between robustness against turbulence, eye-safety requirements, and background noise suppression, with 1550 nm emerging as a favorable wavelength due to its improved coherence parameters and compliance with eye-safety regulations. Similarly, beam waist and aperture optimizations were shown to balance diffraction resilience with coupling efficiency, while raising the receiver above the turbulent ground layer offered moderate improvements under certain conditions.

At the receiver design level, optical subsystems were proposed and integrated into a compact front-end architecture. A Schmidt–Cassegrain telescope is selected with the goal to achieve near diffraction-limited performance while maintaining modularity for auxiliary optics. A quadrant detector should also be used to sense focal-plane displacements with high temporal resolution. This allows real-time feedback to a fast steering mirror for tip/tilt correction. These elements together can remove the dominant low-order turbulence effects and reduce focal spot wander.

While some numerical results may be over or underestimated by the chosen models, the key findings lie in the qualitative trends across scenarios, which show that gains can be achieved by carefully tailoring system parameters and optical architectures to atmospheric conditions. As there are several models originating from different sources, a unified framework to characterize atmospheric effects in satellite QKD more precisely is needed. Future work can examine the consistency of these models experimentally under real turbulence conditions, as well as explore advanced adaptive optics beyond tip/tilt correction. Optimization and prediction algorithms, as well as classical and quantum error correction, may further enhance QKD performance under realistic conditions.

A fiber attenuation and link efficiency

Attenuation in optical fiber is obtained from:

$$\alpha = \frac{10}{L} \log \left(\frac{P_{\text{in}}}{P_{\text{out}}} \right)$$

As transmittance is the ratio between the outout power and the input power:

$$T = \frac{P_{\text{out}}}{P_{\text{in}}}$$

Then:

$$\alpha = -\frac{10}{L} \log(T)$$

And:

$$T = 10^{-\alpha L/10}$$

When $\alpha = 0.1$ dB/km and $L = 1000$ km, this gives:

$$T = 1 \times 10^{-10}$$

References

- [1] Alkholidi Abdulsalam and Altowij Khalil Saeed. Free space optical communications-theory and practices. *Contemporary Issues in Wireless Communications, 1th ed. croatia: intech*, pages 159–212, 2014.
- [2] Valentina Marulanda Acosta. *Quantum Key Distribution through atmospheric turbulence: secure satellite-to-ground links*. PhD thesis, Sorbonne Université, 2023.
- [3] Charles H. Bennett and Gilles Brassard. Quantum cryptography: Public key distribution and coin tossing. *Theoretical Computer Science*, 560:7–11, 2014. Theoretical Aspects of Quantum Cryptography – celebrating 30 years of BB84.
- [4] Alberto Carrasco-Casado, Natalia Denisenko, and Veronica Fernandez. Correction of beam wander for a free-space quantum key distribution system operating in urban environment. *Optical Engineering*, 53(8):084112–084112, 2014.
- [5] Alberto Carrasco-Casado, Verónica Fernández, and Natalia Denisenko. *Free-Space Quantum Key Distribution*, pages 589–607. Springer International Publishing, Cham, 2016.
- [6] Veronica Fernandez, Jorge Gomez-Garcia, Alejandro Ocampos-Guillen, and Alberto Carrasco-Casado. Correction of Wavefront Tilt Caused by Atmospheric Turbulence Using Quadrant Detectors for Enabling Fast Free-Space Quantum Communications in Daylight. *IEEE Access*, 6:3336–3345, 2018.
- [7] Masoud Ghalaii and Stefano Pirandola. Quantum communications in a moderate-to-strong turbulent space. *Communications Physics*, 5(1):38, 2022.
- [8] N. Gisin and R.T. Thew. Quantum communication technology. *Electronics Letters*, 46(14):965–967, July 2010.
- [9] John W Hardy. *Adaptive optics for astronomical telescopes*, volume 16. Oxford university press, 1998.
- [10] N Jovanovic, C Schwab, O Guyon, J Lozi, N Cvetojevic, Frantz Martinache, S Leon-Saval, B Norris, S Gross, D Doughty, et al. Efficient injection from large telescopes into single-mode fibres: Enabling the era of ultra-precision astronomy. *Astronomy & Astrophysics*, 604:A122, 2017.
- [11] Isaac I Kim, Bruce McArthur, and Eric J Korevaar. Comparison of laser beam propagation at 785 nm and 1550 nm in fog and haze for optical wireless communications. In *Optical wireless communications III*, volume 4214, pages 26–37. Spie, 2001.
- [12] Bernard J Klein and John J Degnan. Optical antenna gain. 1: Transmitting antennas. *Applied optics*, 13(9):2134–2141, 1974.
- [13] R Nicholas Lanning, Mark A Harris, Denis W Oesch, Michael D Oliker, and Mark T Gruneisen. Quantum communication over atmospheric channels: a framework for optimizing wavelength and filtering. *Physical Review Applied*, 16(4):044027, 2021.

- [14] Sheng-Kai Liao, Wen-Qi Cai, Wei-Yue Liu, Liang Zhang, Yang Li, Ji-Gang Ren, Juan Yin, Qi Shen, Yuan Cao, Zheng-Ping Li, Feng-Zhi Li, Xia-Wei Chen, Li-Hua Sun, Jian-Jun Jia, Jin-Cai Wu, Xiao-Jun Jiang, Jian-Feng Wang, Yong-Mei Huang, Qiang Wang, Yi-Lin Zhou, Lei Deng, Tao Xi, Lu Ma, Tai Hu, Qiang Zhang, Yu-Ao Chen, Nai-Le Liu, Xiang-Bin Wang, Zhen-Cai Zhu, Chao-Yang Lu, Rong Shu, Cheng-Zhi Peng, Jian-Yu Wang, and Jian-Wei Pan. Satellite-to-ground quantum key distribution. *Nature*, 549(7670):43–47, September 2017.
- [15] Hoi-Kwong Lo, Xiongfeng Ma, and Kai Chen. Decoy state quantum key distribution. *Physical review letters*, 94(23):230504, 2005.
- [16] Chao-Yang Lu, Yuan Cao, Cheng-Zhi Peng, and Jian-Wei Pan. Micius quantum experiments in space. *Rev. Mod. Phys.*, 94:035001, Jul 2022.
- [17] Marco Petrovich, Eric Numkam Fokoua, Yong Chen, Hesham Sakr, Abubakar Isa Adamu, Rosdi Hassan, Dong Wu, Ron Fatobene Ando, Athanasios Papadimopoulos, Seyed Reza Sandoghchi, Gregory Jasion, and Francesco Poletti. Broadband optical fibre with an attenuation lower than 0.1 decibel per kilometre. *Nature Photonics*, September 2025.
- [18] Stefano Pirandola. Satellite quantum communications: Fundamental bounds and practical security. *Physical Review Research*, 3(2):023130, 2021.
- [19] Jeffrey H. Shapiro. Scintillation has minimal impact on far-field bennett-brassard 1984 protocol quantum key distribution. *Phys. Rev. A*, 84:032340, Sep 2011.
- [20] Seok-Min Song, Hyung-Chul Lim, Mansoo Choi, Yu Yi, et al. Analysis of tip/tilt compensation of beam wandering for space laser communication. *Journal of Astronomy and Space Sciences*, 40(4):237–245, 2023.
- [21] Larry B. Stotts and Larry C. Andrews. Improving the Hufnagel-Andrews-Phillips refractive index structure parameter model using turbulent intensity. *Optics Express*, 31(9):14265, April 2023.